

Multi-interface engineering of solar evaporation devices via scalable, synchronous thermal shrinkage and foaming

Kerui Li^a, Minmin Gao^b, Zhipeng Li^b, Haitao Yang^a, Lin Jing^a, Xi Tian^b, Yang Li^a, Shuo Li^a, He Li^a, Qing Wang^c, John S. Ho^b, Ghim Wei Ho^{b,**}, Po-Yen Chen^{a,d,*}

^a Department of Chemical and Biomolecular Engineering, National University of Singapore (NUS), 117585, Singapore

^b Department of Electrical and Computer Engineering, National University of Singapore, 117583, Singapore

^c Department of Materials Science and Engineering, National University of Singapore, 117576, Singapore

^d Department of Chemical and Biomolecular Engineering, University of Maryland, College Park, MD 20742, United States

ARTICLE INFO

Keywords:

Solar evaporation
Multi-interface engineering
Micro-reservoirs
In-plane water transport
Porous substrate
Scalable fabrication

ABSTRACT

Recent years have witnessed continuing advances in solar evaporation technologies to achieve strong synergy among sufficient water supply, efficient light absorption, and favorable heat localization. Still, challenges remain in the fabrication of solar evaporation devices with synergistic performance in a scalable fashion. Herein, we develop a scalable fabrication process involving multi-scale and multi-interface engineering to achieve high-performance and large-area solar evaporation devices. At nanoscale, light-absorbing carbon nanotubes (CNTs) are complexed with hydrophilic cellulose nanofibers (CNFs) to form the nanocomposite inks of CNT-CNF (c-CNT) with tunable viscosity for doctor blading on ethanol-diffused polystyrene (E-PS) films. Through one-step thermal treatment, device shrinkage and substrate foaming are triggered at multi-interfaces to synchronously induce (1) the creation of microscale crumpled c-CNT textures with dual-improved water supply and light absorption and (2) the generation of mesoscale pores in PS substrates with dual-suppressed thermal conduction and radiation. Contributed by the synergistic designs, the solar evaporation device demonstrates a high evaporation rate of $1.41 \text{ kg m}^{-2} \text{ h}^{-1}$ and a conversion efficiency of 95.8% at an extremely low loading of photothermal materials (0.25 mg cm^{-2}). A large-area solar evaporation panel is realized to highlight the practical consideration toward more impactful solar evaporation exploitation.

1. Introduction

As one of the promising renewable energy sources, solar energy has been constantly pursued to be efficiently harvested to satisfy the daily needs of human activities and offer a solution for the increasing energy crisis. Among many emerging solar energy technologies, solar evaporation attracted tremendous attention due to its simple device structure, high conversion efficiency, and easy operation, promising wide applications including seawater desalination, sewage treatment, and electricity generation [1–3]. Recently, through the development of photothermal materials and the optimization of device interfaces, continuing efforts have been made in various device configurations to achieve the synergy among sufficient water supply, efficient light absorption, and favorable heat localization for high-performance solar evaporation [4–6].

Still, it remains challenging to develop a scalable fabrication technique for the high-performance solar evaporation devices that exhibit strong synergy among three categories mentioned above [7–9]. One approach is to utilize three-dimensional (3D) porous structures (e.g., aerogels) with efficient light absorption, low thermal conductivity, and sufficient through-plane water channels, enabling the fabrication of solar evaporation devices with synergistic performance [10–12]. Recently, further coupled with the energy-harvesting capability from the environment or the ability to reduce the latent heat of water evaporation, some unconventional 3D devices demonstrated improved solar evaporation performance [13–15]. However, these 3D device configurations were normally composed of porous, centimeter-thick solar-thermal conversion layers with high areal loadings of photothermal materials, thus resulting in high material costs as well as low mechanical stability [8]. Moreover, the fabrication of several 3D devices involved

* Corresponding author. Department of Chemical and Biomolecular Engineering, National University of Singapore (NUS), 117585, Singapore.

** Corresponding author.

E-mail addresses: lehgw@nus.edu.sg (G.W. Ho), checp@nus.edu.sg (P.-Y. Chen).

complex, time-consuming, and cost-ineffective processes (e.g., freeze-drying or chemical vapor deposition), which led to high production costs and limited their large-scale manufacture.

Another widely-utilized device configuration for solar evaporation is based on a bilayer structure constructed with a thin solar-thermal conversion layer on a thermal insulation substrate [16–18]. With strong mechanical support from the substrates beneath, various printing techniques can be utilized to deposit the nano-/micro-meter-thick solar-thermal conversion layers [19–21], presenting high potential in the scalable fabrication of solar evaporation devices. However, several challenges are required to be addressed for their future manufacture. First, the upper solar-thermal conversion layers were ultrathin and possessed narrow water channels with limited in-plane water supply. Second, the upper layers exhibited relatively low areal loadings of photothermal materials and generally suffered from moderate light reflection/transmission, resulting in inefficient light absorption. An evident trade-off between the loading of relatively pricy photothermal materials and the performance of solar evaporation devices was observed in the bilayer devices, where inefficient water transport and light absorption happened. Besides the trade-off on upper layers, further structural designs were highly required for the thermal insulation substrates beneath to prevent unfavorable heat dissipation as well as to achieve the synergistic performance mentioned above.

To address these challenges, a scalable fabrication process that involved multi-scale and multi-interface engineering was developed to achieve large-area solar evaporation devices in bilayer configurations (Scheme 1). At nanoscale, carbon nanotubes (CNTs) with efficient photothermal capabilities were first complexed with hydrophilic cellulose nanofibers (CNFs) to form CNT-CNF nanocomposites (abbreviated as c-CNTs). The dual-functional c-CNTs were well dispersed in water to form rheologically-tunable aqueous inks for various printing techniques. Next, the high-viscosity c-CNT ink was uniformly coated on an ethanol-diffused polystyrene (E-PS) film *via* a doctor-blading method. Followed by one-step thermal treatment, device shrinkage and substrate foaming were triggered synchronously for the scalable fabrication of solar evaporation devices. At microscale, because of the thermal shrinkage of E-PS substrate, the coated c-CNT layer was deformed at solid-solid (c-CNT-PS) interface to form the crumple-textured structures with dual-

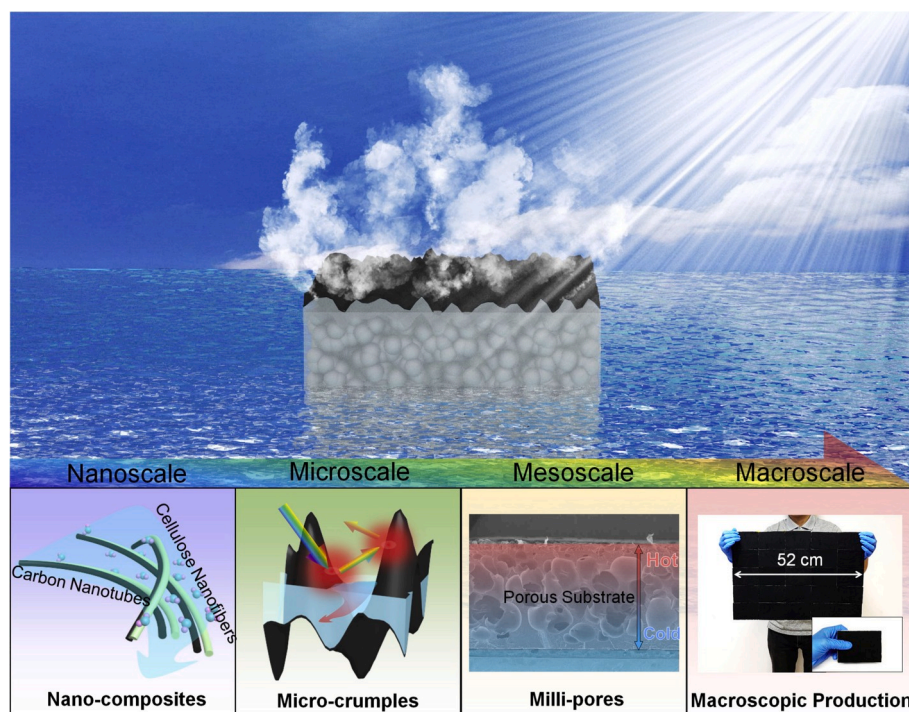
improvement on water supply and light absorption. At mesoscale, the thermal foaming at gas-solid (ethanol vapor-PS) interface was implemented *via* the evaporation of pre-diffused ethanol to generate porous PS substrates with dual-suppression in thermal conduction and radiation for favorable heat localization. Contributed by the synergistic designs, the solar evaporation device demonstrated a high evaporation rate of $1.41 \text{ kg m}^{-2} \text{ h}^{-1}$ and a conversion efficiency of 95.8% at an extremely low c-CNT loading of 0.25 mg cm^{-2} and a low material cost (detailed cost calculation and comparison in Note S1 and S2). Because of the scalable multi-interface engineering approach, a large-area solar evaporation panel (accompanied with a model house for condensate water collection) was realized to highlight the practical consideration toward more impactful solar evaporation exploitation.

2. Results and discussion

2.1. Scalable fabrication of solar evaporation devices via doctor-blading followed by one-step thermal treatment

Fig. 1a demonstrates the scalable fabrication process of solar evaporation devices *via* doctor blading followed by one-step thermal treatment. First, the E-PS films were secured on an automatic film coater, and the doctor blade was moved across the entire E-PS films to spread out the c-CNT paste with optimized concentration and viscosity. After being air-dried, a large-area c-CNT nanocoating ($42 \times 21 \text{ cm}$) with the thickness of ca. 460 nm was obtained on the E-PS films (Fig. S1a). Then, the c-CNT-coated device was treated at $135 \text{ }^\circ\text{C}$ (see detailed discussion regarding temperature optimization in Note S3) to induce the interfacial engineering at solid-solid (c-CNT nanocoating-PS) and gas-solid (ethanol vapor-PS) interfaces simultaneously (as illustrated in Fig. S1b), and finally lead to synchronous thermal shrinkage and foaming of E-PS films (as shown in Movie S1). It should be mentioned that the solar evaporation device in right inset of Fig. 1a was assembled by three pieces of smaller devices and such fabrication process can be scaled up to achieve a much larger-sized solar evaporation device by using industry-level equipment.

Supplementary data related to this article can be found at <https://doi.org/10.1016/j.nanoen.2020.104875>.



Scheme 1. Multi-scale and multi-interface engineering for large-area solar evaporation devices in bilayer configurations. At nanoscale, light-absorbing CNTs were complexed with hydrophilic CNFs to achieve c-CNTs. At microscale, crumple-textured c-CNT structures were fabricated through thermal shrinkage at solid-solid (c-CNT nanocoating-PS) interface, demonstrating sufficient in-plane water supply and improved light absorption. At mesoscale, milli-scale pores were developed within PS substrates through thermal foaming at gas-solid (ethanol vapor-PS) interface, showing improved thermal insulation capability. At macroscale, contributed by synergistic designs of device configurations and synchronous multi-interface engineering, a large-area and portable solar evaporation panel was realized *via* doctor blading followed by one-step thermal treatment.

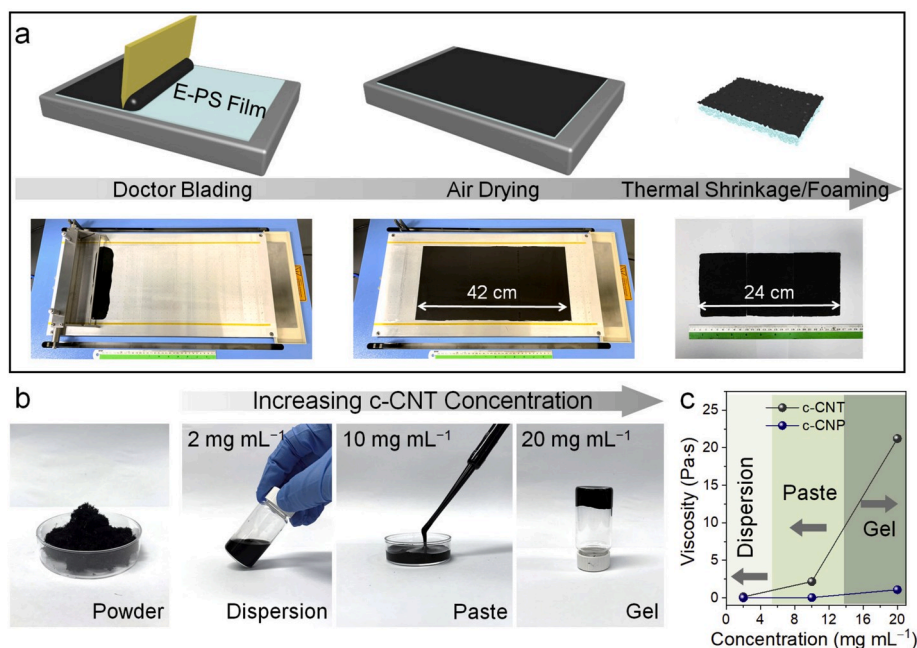


Fig. 1. Fabrication of solar evaporation devices *via* doctor-blading of c-CNT paste followed by one-step thermal treatment. (a) Schematic illustration (top) and digital photographs (bottom) of the fabrication process. (b) Digital photographs of pristine CNT powders, dilute c-CNT dispersion, viscous c-CNT paste, and self-standing c-CNT gel, showing tunable rheology of c-CNT aqueous inks. (c) Viscosities of c-CNT and c-CNP inks at a shear rate of 1° s^{-1} as a function of c-CNT and c-CNP loadings.

In this fabrication process, suitable photothermal materials should be first explored and carefully selected based on the standards of light-to-heat conversion efficiency, processability, surface hydrophilicity, and material cost. CNTs with broadband light absorption have been regarded as one promising solar-thermal conversion material [16,22]. However, problems still existed in their large-scale solution processing, such as poor dispersity, environmental unfriendliness, and complicated procedures (see detailed discussion in **Note S4**) [23–25]. Here, CNF was selected as a stable polymer surfactant to disperse pristine CNTs in aqueous solutions as well as to provide effective hydrophilic modification on CNTs. As shown in **Fig. S2**, CNFs displayed typical one-dimensional (1D) morphology. Upon sufficient energy provided by ultrasonication, pristine CNT aggregates were separated and gradually complexed with CNFs, where the attraction force originated from the interactions between the counterions on CNFs and the polarized electrons of CNTs [26]. After the complexation with CNTs, the carboxyl groups on CNFs tended to dissociate into negatively charged carboxylates (zeta potential: ca. -54.6 mV) [27], leading to electrostatically stable c-CNTs in aqueous solutions. Both multi-walled (MCNTs) and single-walled carbon nanotubes (SCNTs) can be complexed with CNFs to form c-MCNTs and c-SCNTs, respectively, as shown in **Fig. S3**. In contrast, without adding CNFs, CNTs quickly aggregated due to their strong van der Waals interactions and poor electrostatic repulsion (**Fig. S4**).

With the incorporation of CNFs, as the loading of c-CNTs increased, the state of c-CNT inks gradually transitioned from a low-viscosity dispersion to a thick, viscous paste, and finally to a self-standing gel (**Fig. 1b**). As the c-MCNT loading reached 10 mg mL^{-1} (consisting of 5 mg mL^{-1} of CNFs and 5 mg mL^{-1} of MCNTs), a viscous c-MCNT paste was obtained without distinct aggregates, where c-MCNTs were highly interconnected into a percolation network. The viscous paste exhibited a typical shear-thinning behavior (**Fig. S5a**), making it suitable for large-area doctor blading. The c-MCNT paste was able to be spread out under large shear stress and uniformly coated on E-PS films by doctor blading, yielding a continuous c-MCNT nanocoating. Similarly, with the incorporation of CNFs, c-SCNT inks were also achieved with tunable viscosity (**Figs. S5b and c**). Compared with CNTs, carbon nanoparticles (CNPs) were difficult to form a similar percolation network after the incorporation with CNFs,

presenting poor viscosity tunability in the resulting CNF–CNP nanocomposites (called c-CNPs) (**Fig. S6**). As shown in **Fig. 1c**, even at a high c-CNP concentration of 10 mg mL^{-1} , the c-CNP dispersion exhibited low viscosity ($0.048 \text{ Pa}\cdot\text{s}$) and was not suitable as a processable ink for doctor blading (**Fig. S6c**), showing the synergy between CNTs and CNFs.

2.2. Engineering at solid-solid interface to generate crumpled textures for dual-improvement of water supply and light absorption

With the printable c-CNT paste, a large-area, hydrophilic, planar c-CNT nanocoating was obtained *via* doctor blading on E-PS films. However, there are two issues of using such planar nanocoating for large-area solar evaporation applications. First, planar nanoscale-thick coatings suffer from poor in-plane water supply due to their narrow water channels. Second, moderate light reflection results from the difference of refractive indices between air (n_1) and c-CNT nanocoating (n_2), according to the Fresnel equation under a normal incidence situation, $R = \left(\frac{n_1 - n_2}{n_1 + n_2}\right)^2$.

To improve water supply and sunlight absorption jointly, the solid-solid interface between c-CNT active layer and E-PS film was engineered by harnessing surface instability during the contraction of thermally-responsive E-PS substrate. As shown in **Fig. 2a** and **Fig. S7**, through the thermal shrinkage of E-PS films, crumple-textured c-CNT nanocoatings were produced with an average peak-to-peak distance of ca. $40 \mu\text{m}$. With the higher dimensional structures, the deformed c-CNT nanocoatings allowed sufficient water supply across the entire active layer, which is an essential design principle especially for large-area solar evaporation devices. To verify the mechanism of sufficient water supply on crumple-textured active layers, surface hydrophilicity of crumpled c-MCNT nanocoatings was first investigated and compared with planar MCNT, crumpled MCNT, and planar c-MCNT nanocoatings. As shown in **Fig. 2b** and **Fig. S8**, without the CNF modification, both planar and crumpled MCNT nanocoatings were hydrophobic and exhibited high water contact angles of $>90^\circ$. In comparison, with the incorporation of hydrophilic CNFs (**Fig. S9a**), both planar and crumpled c-MCNT nanocoatings were hydrophilic, and the water contact angles

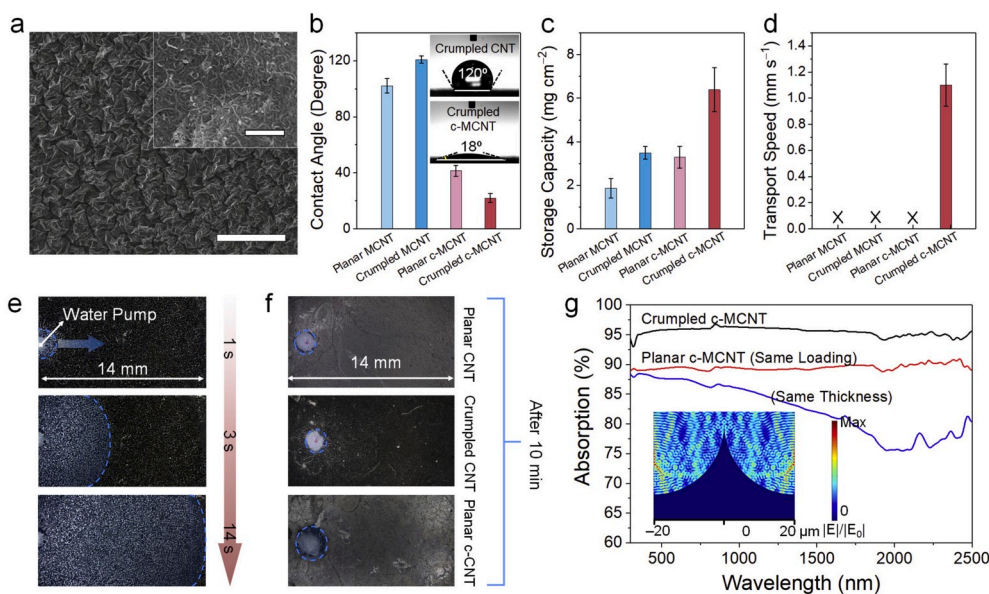


Fig. 2. Engineering at solid-solid interface via thermal shrinkage to generate crumpled c-CNT textures for dual water supply and light absorption functions. (a) SEM images of crumple-textured c-MCNT nanocoating (scale bar: 500 μm). The inset is an enlarged SEM image, showing an interconnected nano-tube/-fiber c-MCNT network (scale bar: 500 nm). (b) Water contact angles of different nanocoatings with the same areal mass loading of ca. 0.25 mg cm^{-2} . (c) Water storage capacities of different nanocoatings after 30-s immersion in water. (d) Water transport speeds on different types of nanocoatings. (e) Microscopic images of a crumpled c-MCNT nanocoating with cotton yarn as a water pump, demonstrating rapid in-plane water transport. The dark grey and blue-colored sections are the dry and wet region respectively. (f) Microscopic conversion images after pumping water through cotton yarn for 10 min. (g) Light absorption spectra of crumpled and planar c-MCNT nanocoating (0.25 mg cm^{-2} , 460 nm). The inset is simulated electric field distribution of the crumpled structures at a wavelength of 1,500 nm.

largely decreased to 42° and 18° , respectively, which ensured their better surface wettability (Figs. S9b and c). In addition, the crumpled c-MCNT structures with high hydrophilicity further allowed water to be stored in their valley regions, serving as the microscale reservoirs to ensure sufficient water storage (details in Fig. S9c). As shown in Fig. 2c, the crumpled c-MCNT nanocoating demonstrated a much higher capacity for water adsorption (6.38 mg cm^{-2} ; weight ratio of ca. 24 g g^{-1} between water and c-MCNTs) than those of other nanocoatings, which was even higher than the saturated water contents of some hydrogels in the literature [28–31].

At last, the crumpled c-MCNT nanocoatings showed significantly improved in-plane water transport, since the crumpled textures served as numerous micro-reservoirs to store water and to connect water channels, similar as the operation mode of neural networks. To investigate the in-plane water transport behaviors, one small open hole (ca. 1.0 mm in diameter) was drilled on each device, and cotton yarn was threaded to pump water from the pool below, as illustrated in Fig. S9d. The crumpled c-MCNT nanocoating allowed water to quickly spread out and cover entire circular area with the diameter of 30 mm; the in-plane water transport speed was estimated to be ca. 1.1 mm s^{-1} (Fig. 2d and e and Movie S2). In contrast, water was not able to spread across either planar or crumpled MCNT nanocoating (Fig. 2f). Although the planar c-MCNT nanocoating was hydrophilic, water was not able to spread out the entire nanocoating due to the nanoscale-thick water channels.

Supplementary video related to this article can be found at <https://doi.org/10.1016/j.nanoen.2020.104875>

Besides sufficient water supply, the crumple-textured c-CNT structures allowed incident sunlight to experience scattering and multiple internal reflections, which largely suppressed unfavored light reflection and transmission (Fig. S10) and thus improved light absorption. As shown in Fig. 2g, because of moderate light reflection, the planar c-MCNT nanocoating with the same areal loading (0.25 mg cm^{-2}) showed an average light absorption of 89.5% and a solar absorption of 89.3%. For the planar c-MCNT sample with the same thickness (460 nm, areal loading of 0.08 mg cm^{-2}), light was not only reflected but also went through the planar nanocoating due to reduced loading of active materials, leading to further decreased light absorption of 82.4% (86.0% in solar absorption). In comparison, the crumpled c-MCNT nanocoating showed an increased average absorption of 95.5% (i.e., 95.9% in solar absorption) through scattering and reflecting incident light in the

crumpled structures to avoid light reflection and transmission [19,32], which was further theoretically verified by our optical simulation results (Fig. S11a). The simulated electric field (E-field) maps showed widely spread hot spots around the crumpled structure compared with those of the planar structure (the inset of Fig. 2g and Figs. S11b and c), where the confinement of E-fields was induced by strong localized surface plasmon resonances [19,33,34]. The increased light absorption eventually resulted in improved light-to-heat performance under one-sun illumination, where the equilibrium temperature of crumpled c-MCNT nanocoating was ca. 2.8°C -higher than that of planar control with the same areal mass loading and ca. 4.9°C -higher than that with the same thickness (Fig. S10d).

2.3. Engineering at gas-solid interface to generate porous substrates for dual-suppression of thermal conduction and radiation

Besides the creation of crumpled c-CNT textures, porous PS substrates were synchronously constructed as the heat-insulating substrates to inhibit possible heat dissipation from the upper active layers for optimized solar-thermal conversion (Fig. 3a). Here, an unconventional foaming agent, ethanol, was introduced into thermally-responsive PS films through simple ethanol diffusion prior to the deposition of c-CNT layers. We have also explored other common organic solvents and found that ethanol was the best foaming agent to produce large pores (see details in Fig. S12).

Through the vaporization of diffused ethanol in PS matrix, the internal vapor pressure was gradually built up for the generation of large pores within shrunk PS substrates. As shown in Fig. 3b,c and Fig. S13a, the pore size and porosity of shrunk PS substrates were controlled through the soaking time in ethanol. When the soaking time increased from 4 to 12 days, the average sizes of generated pores increased from ca. 0.3–0.7 mm, and the porosity increased from 19.3% to 65.4%, conducive to the decrease of through-plane thermal conductivity [35]. Moreover, after thermal foaming, the mass densities of porous PS substrates gradually decreased from ca. 1.04 to 0.36 g cm^{-3} (Fig. 3d), enabling the solar evaporation devices to easily float on water and to facilitate the heat localization on c-CNT nanocoatings.

The mechanism of thermal foaming was further examined by Fourier transform infrared (FTIR) spectroscopy and thermogravimetric analysis (TGA). As shown in Fig. 3e, the E-PS sample presented a remarkable

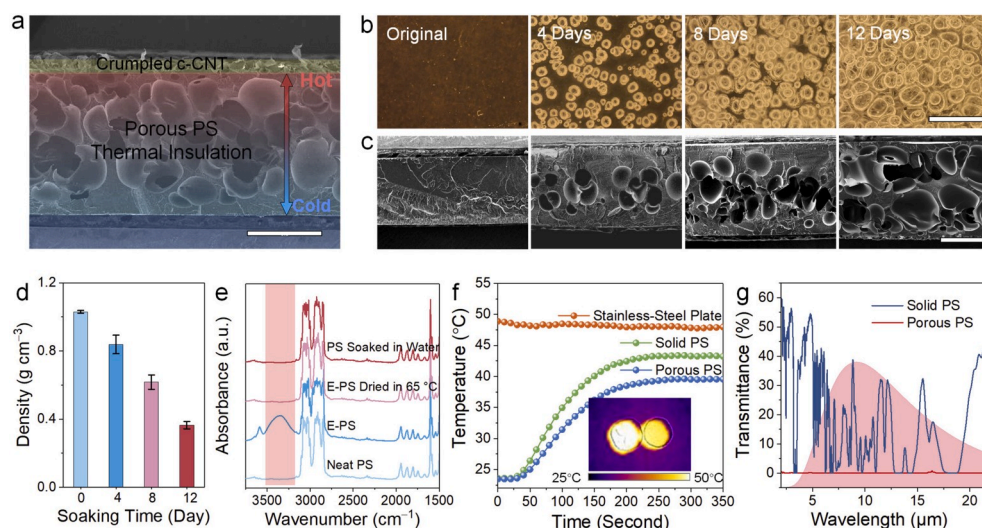


Fig. 3. Engineering at gas-solid interface via thermal foaming to generate porous PS substrates for dual-suppression of thermal conduction and radiation. (a) Cross-sectional SEM image of porous PS substrates with improved thermal insulation (scale bar: 1 mm). (b) Top-view microscopic images (scale bar: 2 mm) and (c) cross-sectional SEM (scale bar: 1 mm) images of porous PS substrates fabricated by using E-PS films that were soaked in ethanol for different durations. (d) Densities of porous PS substrates that were soaked in ethanol for different durations. (e) FTIR spectra of different types of PS and E-PS films, showing different characteristic absorption peaks ($-OH$ groups highlighted in red). (f) Surface temperature profiles of solid and porous PS substrates (with the same thickness) on a hotplate covered with a polished stainless-steel plate. The inset is a thermal image of solid and porous PS substrates at their equilibrium temperatures. (g) Transmittance spectra of solid and porous PS substrates at infrared wavelengths. The red-shaded area represents the black-body radiation at 42 °C.

absorption peak of ca. $3,350\text{ cm}^{-1}$, corresponding to the O–H stretching vibrations of ethanol molecules. In comparison, neither neat PS nor heated E-PS at 65 °C displayed a similar absorption peak at $3,350\text{ cm}^{-1}$. The PS film soaked in water for 12 days did not present such characteristic peak either, indicating that water or humidity was less likely to involve in the pore-generation mechanism. Moreover, in the TGA profile (Fig. S13b), as the temperature increased to ca. 75 °C (near the boiling point of ethanol), the weight of E-PS samples sharply decreased. In contrast, either neat PS or heated E-PS samples show noticeable weight loss.

Next, the thermal insulation capability of porous PS substrates was systemically investigated in two aspects: thermal conduction and radiation. We placed 2.5-mm-thick solid (without foaming) and foamed PS substrates on a heated stainless-steel plate (48 °C), and their upper surface temperatures were measured in real time as illustrated Fig. S14a. As shown in Fig. 3f, the porous PS substrate exhibited a lower surface temperature of 39.5 °C than that of the solid PS substrate (43.3 °C), demonstrating that the porous PS substrates efficiently suppressed the through-plane thermal conduction (also verified by the thermal images in Fig. S14b). The experimental results were consistent with the conclusion of thermal dynamic simulation (Fig. S15a).

Besides, thermal radiation was studied in the infrared range (from 2.5 to 25 μm), where the black-body radiation at 42 °C (the temperature of c-CNT layer during solar evaporation) mainly existed according to Planck's law. As shown in Fig. S15b, because of limited chemical groups of PS substrate (e.g., aromatic C–H, alkyl C–H, and aromatic C=C) for vibration absorption, the solid PS substrate exhibited discontinuous absorption peaks, leading to partial transmission of thermal radiation in the infrared range (Fig. 3g). The transmitted thermal radiation would be absorbed by bulk water beneath if there is no suitable insulation provided, which is disadvantageous to the heat localization on the upper c-CNT layer. With the generated pores in PS substrate, the thermal radiation was scattered and reflected at the internal gas-solid interfaces, leading to a negligible transmittance in the infrared range (Fig. 3g) and thus providing sufficient insulation of thermal radiation.

2.4. High-efficiency and large-area solar evaporation

To evaluate the effect of our multi-interface and multi-scale designs on the solar evaporation performance, the custom-built device composed of a crumpled c-MCNT nanocoating and a porous PS substrate

with the optimal thickness of 2.5 mm (detailed optimization of substrate thickness in Note S5) was tailored with the diameter of 3.3 cm as shown in the inset in Fig. S16a (abbreviated as CM-PP device hereafter). The UV–vis–NIR absorption spectra of a crumpled c-MCNT nanocoating were measured under its dry and wet states, respectively, and did not show obvious changes (Fig. S16b). Under one-sun illumination, the CM-PP device showed high evaporation rates and solar energy conversion efficiencies (η) of $1.41\text{ kg m}^{-2}\text{ h}^{-1}$ and 95.8% at 30 °C and the relative humidity (RH) of 40% (See details in Note S6), and of $1.30\text{ kg m}^{-2}\text{ h}^{-1}$ and 89.2% at 23 °C and the RH of 65% (Fig. 4a and Table S1) [20,21,36].

The crumpled c-CNT textures are essential for the solar-thermal conversion layers to achieve sufficient water supply and improved sunlight absorption under low loadings of photothermal materials. As shown in Fig. 4b, i, under one-sun illumination, the CM-PP device showed continuous water supply to wet entire c-MCNT layer over 180 min (detailed comparison in Fig. S17a). Compared with the CM-PP device at 23 °C and the RH of 65%, for the device with planar c-MCNT layer, the surface was initially wet and quickly dried within 30 min (Fig. 4b, ii), which was consistent with the results in Fig. 2. Coupled with moderate light reflection, the device with planar c-MCNT layer exhibited a lower evaporation rate of $0.82\text{ kg m}^{-2}\text{ h}^{-1}$ and a conversion efficiency of 56.2%. Neither planar nor crumpled MCNT surfaces exhibited sufficient water supply for solar evaporation (Fig. 4b, iii, iv), and non-wetting regions were observed on both devices. Therefore, the devices with planar and crumpled MCNT active layers also showed low evaporation rates of 0.47 and $1.06\text{ kg m}^{-2}\text{ h}^{-1}$ as well as low conversion efficiencies of 32.2% and 72.7%, respectively (Table S1).

Subsequently, to verify the advantages of using porous substrates, the solar evaporation devices with different PS substrates (all with crumpled c-MCNT layers) were investigated in Fig. 4c. As expected, because of the dual-suppression in thermal conduction and radiation, the CM-PP device reached an evaporation rate of $1.30\text{ kg m}^{-2}\text{ h}^{-1}$ and a conversion efficiency of 89.2% (at 23 °C and the RH of 65%), which were higher than the device with a 2.5-mm-thick solid PS substrate ($1.20\text{ kg m}^{-2}\text{ h}^{-1}$ and 82.3%). We also tested the device without substrate (crumpled c-MCNT layers only), which showed a lower evaporation performance ($1.06\text{ kg m}^{-2}\text{ h}^{-1}$ and 72.6%). As shown in Fig. 4d and Fig. S17b, during 30-min illumination, the water temperatures right beneath the CM-PP device and at 5-cm depth increased by 4.4 and 2.5 °C over bulk water, respectively. The thermal image in Fig. S17c further

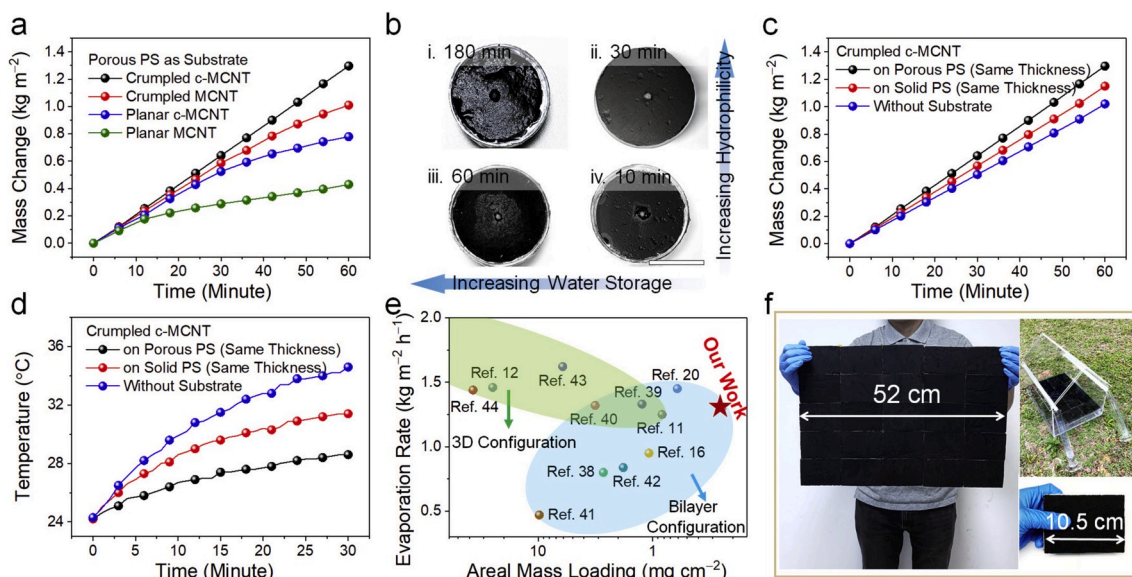


Fig. 4. High-efficiency and large-area solar evaporation. (a) Mass changes of water over time for the solar evaporation devices with different solar–thermal conversion layers on porous PS substrates under one-sun illumination. (b) Water supply phenomena on the surfaces of (i) crumpled c-MCNT layer for 180 min, (ii) planar c-MCNT layer for 30 min, (iii) crumpled MCNT layer for 60 min, and (iv) planar MCNT layer for 10 min (scale bar: 2 cm). (c) Mass changes of water over time for the solar evaporation devices with crumpled c-MCNT layers on different types of substrates. (d) Temperature evolution of water bath beneath different solar evaporation devices. (e) Comparison between our CM-PP device and the reported solar evaporation devices in terms of the areal mass loadings of active materials and the evaporation rates. (f) Photograph of a large-area solar evaporation panel. The top inset is the setup for outdoor solar evaporation and condensate water collection, and the bottom inset is a photograph of stacked and portable solar evaporation devices disassembled from the large-area panel.

demonstrated the solar light-converted heat was localized on the crumpled c-MCNT layer of CM-PP device for water evaporation. In comparison, the device with solid PS substrate (7.2 and 3.7 °C) and with crumpled c-MCNT layer only (10.3 and 5.1 °C) exhibited poorer thermal insulation performance, showing larger temperature increases. Furthermore, the CM-PP device was operated in simulated (an aqueous solution with 3.5 wt% NaCl) and real seawater, and acidic and alkaline solutions to investigate its potential in solar desalination and sewage treatment (see detailed discussion in Fig. S18) [37].

Notably, besides high solar evaporation performance demonstrated by CM-PP devices, our multi-interface engineering approach introduced two additional advantages for practical applications, including (1) low areal loading of photothermal materials for reduced material cost and (2) scalable fabrication processes for industrial-level production. Generally, high areal loadings of photothermal materials (more than 1 mg cm⁻² in most of the literature) were required to ensure sufficient light absorption and efficient solar–thermal conversion for high-performance solar evaporation, which may result in high material cost and thus limit practical applications. In comparison, our CM-PP device required a much lower areal loading of active materials (0.25 mg cm⁻²) and still guaranteed a relatively high evaporation rate (Fig. 4e and Table S2) [11–13,16,20,38–44]. The material cost of a CM-PP device was estimated to be ca. 5.4 USD m⁻² and could be further reduced to 1.3 USD m⁻² in mass manufacture, showing high competitiveness in industrial applications (detailed cost calculation and comparison in Note S1 and S2).

Additionally, through scalable doctor blading and synchronous thermal shrinkage/foaming, a large quantity of CM-PP devices were easily produced and further assembled into a large-area panel for practical solar evaporation applications. A CM-PP device with the area of ca. 100 cm² was prepared and tested under outdoor conditions (Figs. S19a and b). From 12:00 to 14:00, the device produced 26.6 g of vapor and showed a conversion efficiency of ca. 90.3% (solar flux density: ca. 1.0 kW m⁻²; temperature: ca. 31 °C; humidity: ca. 74%), similar as the performance of small-scale CM-PP devices measured in lab conditions. Furthermore, a large-area panel of CM-PP devices (ca. 1,900

cm²) was achieved by assembling 25 devices together by using polyimide (PI) tapes for practical solar evaporation demonstration (Fig. 4f). Here, a model house was constructed using transparent acrylic plates with a roof to condensate the vapor and accumulate water droplets to the collection troughs (the top inset in Fig. 4f). Under the natural light radiation with solar flux density of ca. 0.95 kW m⁻² from 12:00 to 14:00 (Fig. S19c), 101 mL of condensate water was collected by using the large-area panel. Additionally, the large-area panel was able to be disassembled into portable small pieces, thus facilitating the loading, moving, and washing processes of the large-area panel as well as providing mobile clean water production (the bottom inset in Fig. 4f) [45].

3. Conclusion

In summary, we developed a multi-interface engineering to realize synergistic structural designs of micro-scale crumpled textures and light absorption and mesoscale pores for ensuring efficient solar evaporation performance. Moreover, our work included two accompanied advantages for practical exploitation. First, contributed by rheologically-tunable c-CNT inks and scalable fabrication process, large-area solar evaporation devices (ca. 1,900 cm²) can be realized through the doctor-blading method and one-step thermal treatment. Second, the crumpled-textured solar–thermal conversion layers guaranteed sufficient water supply and high light absorption under an extremely low material loading (0.25 mg cm⁻²) and relatively low cost for future manufacture.

Declaration of competing interest

The authors declare that they have no known competing financial interests or personal relationships that could have appeared to influence the work reported in this paper.

Acknowledgment

The authors acknowledge the financial support provided by the

Faculty Research Committee (FRC) Start-Up Grant of National University of Singapore R-279-000-515-133, the Ministry of Education Academic Research Fund (AcRF) R-279-000-538-114, R-279-000-532-114, R-279-000-551-114, R-397-000-227-112, the AME Young Investigator Research Grant R-279-000-546-305 (A*STAR Grant No. A1884c0017), and the Singapore-MIT Alliance for Research and Technology (SMART) Ignition Grant R-279-000-572-592.

Appendix A. Supplementary data

Supplementary data to this article can be found online at <https://doi.org/10.1016/j.nanoen.2020.104875>.

References

- [1] F. Zhao, X. Zhou, Y. Shi, X. Qian, M. Alexander, X. Zhao, S. Mendez, R. Yang, L. Qu, G. Yu, *Nat. Nanotechnol.* 13 (2018) 489–495.
- [2] J. Zhou, Y. Gu, P. Liu, P. Wang, L. Miao, J. Liu, A. Wei, X. Mu, J. Li, J. Zhu, *Adv. Funct. Mater.* 29 (2019), 1903255.
- [3] L. Zhu, M. Gao, C.K.N. Peh, G.W. Ho, *Mater. Horiz.* 5 (2018) 323–343.
- [4] X. Li, G. Ni, T. Cooper, N. Xu, J. Li, L. Zhou, X. Hu, B. Zhu, P. Yao, J. Zhu, *Joule* 2 (2019) 1–8.
- [5] P. Tao, G. Ni, C. Song, W. Shang, J. Wu, J. Zhu, G. Chen, T. Deng, *Nat. Energy* 3 (2018) 1031–1041.
- [6] S.B. Darling, *J. Appl. Phys.* 124 (2018), 030901.
- [7] C. Chen, Y. Kuang, L. Hu, *Joule* 3 (2019) 683–718.
- [8] X. Zhou, Y. Guo, F. Zhao, G. Yu, *Acc. Chem. Res.* 52 (2019) 3244–3253.
- [9] Y. Liu, S. Yu, R. Feng, A. Bernard, Y. Liu, Y. Zhang, H. Duan, W. Shang, P. Tao, C. Song, T. Deng, *Adv. Mater.* 27 (2015) 2768–2774.
- [10] Z.-J. Xia, H.-C. Yang, Z. Chen, R.Z. Waldman, Y. Zhao, C. Zhang, S.N. Patel, S. B. Darling, *Adv. Mater. Interfaces* 6 (2019), 1900254.
- [11] Y. Li, T. Gao, Z. Yang, C. Chen, W. Luo, J. Song, E. Hitz, C. Jia, Y. Zhou, B. Liu, B. Yang, L. Hu, *Adv. Mater.* 29 (2017), 1700981.
- [12] Q. Zhang, G. Yi, Z. Fu, H. Yu, S. Chen, X. Quan, *ACS Nano* 13 (2019) 13196–13207.
- [13] Y. Guo, X. Zhou, F. Zhao, J. Bae, B. Rosenberger, G. Yu, *ACS Nano* 13 (2019) 7913–7919.
- [14] W. Li, Z. Li, K. Bertelsmann, D.E. Fan, *Adv. Mater.* 31 (2019), 1900720.
- [15] Y. Bian, Q. Du, K. Tang, Y. Shen, L. Hao, D. Zhou, X. Wang, Z. Xu, H. Zhang, L. Zhao, S. Zhu, J. Ye, H. Lu, Y. Yang, R. Zhang, Y. Zheng, S. Gu, *Adv. Mater. Technol.* 4 (2019), 1800593.
- [16] C. Chen, Y. Li, J. Song, Z. Yang, Y. Kuang, E. Hitz, C. Jia, A. Gong, F. Jiang, J. Y. Zhu, B. Yang, J. Xie, L. Hu, *Adv. Mater.* 29 (2017), 1701756.
- [17] N. Xu, J. Li, Y. Wang, C. Fang, X. Li, Y. Wang, L. Zhou, B. Zhu, Z. Wu, S. Zhu, *J. Zhu, Sci. Adv.* 5 (2019) eaaw7013.
- [18] H.-C. Yang, Z. Chen, Y. Xie, J. Wang, J.W. Elam, W. Li, S.B. Darling, *Adv. Mater. Interfaces* 6 (2019), 1801252.
- [19] K. Li, T.-H. Chang, Z. Li, H. Yang, F. Fu, T. Li, J.S. Ho, P.-Y. Chen, *Adv. Energy Mater.* 9 (2019), 1901687.
- [20] X. Li, W. Xu, M. Tang, L. Zhou, B. Zhu, S. Zhu, J. Zhu, *Proc. Natl. Acad. Sci. U. S. A.* 113 (2016) 13953–13958.
- [21] M. Zhu, Y. Li, F. Chen, X. Zhu, J. Dai, Y. Li, Z. Yang, X. Yan, J. Song, Y. Wang, E. Hitz, W. Luo, M. Lu, B. Yang, L. Hu, *Adv. Energy Mater.* 8 (2018), 1701028.
- [22] Y. Wang, L. Zhang, P. Wang, *ACS Sustain. Chem. Eng.* 4 (2016) 1223–1230.
- [23] K. Chiou, S. Byun, J. Kim, J. Huang, *Proc. Natl. Acad. Sci. U. S. A.* 115 (2018) 5703–5708.
- [24] C.A. Furtado, U.J. Kim, H.R. Gutierrez, L. Pan, E.C. Dickey, P.C. Eklund, *J. Am. Chem. Soc.* 126 (2004) 6095–6105.
- [25] K.A. Wepasnick, B.A. Smith, K.E. Schrote, H.K. Wilson, S.R. Diegelmann, D. H. Fairbrother, *Carbon* 49 (2011) 24–36.
- [26] A. Hajian, S.B. Lindström, T. Pettersson, M.M. Hamed, L. Wagberg, *Nano Lett.* 17 (2017) 1439–1447.
- [27] T. Li, S.X. Li, W. Kong, C. Chen, E. Hitz, C. Jia, J. Dai, X. Zhang, R. Briber, Z. Siwy, M. Reed, L. Hu, *Sci. Adv.* 5 (2019), eaau4238.
- [28] X. Zhou, F. Zhao, Y. Guo, B. Rosenberger, G. Yu, *Sci. Adv.* 5 (2019), eaaw5484.
- [29] D.K. Nandakumar, Y. Zhang, S.K. Ravi, N. Guo, C. Zhang, S.C. Tan, *Adv. Mater.* 31 (2019), 1806730.
- [30] M. Tan, J. Wang, W. Song, J. Fang, X. Zhang, *J. Mater. Chem.* 7 (2019) 1244–1251.
- [31] V.R. Feig, H. Tran, M. Lee, Z. Bao, *Nat. Commun.* 9 (2018) 2740.
- [32] S. Zeng, D. Zhang, W. Huang, Z. Wang, S.G. Freire, X. Yu, A.T. Smith, E.Y. Huang, H. Nguon, L. Sun, *Nat. Commun.* 7 (2016) 11802.
- [33] T. Morimoto, S.-K. Joung, T. Saito, D.N. Futaba, K. Hata, T. Okazaki, *ACS Nano* 8 (2014) 9897–9904.
- [34] H. Butt, Q. Dai, R. Rajesekharan, T.D. Wilkinson, G.A.J. Amarantunga, *ACS Nano* 5 (2011) 9138–9143.
- [35] J. Skibinski, K. Cwieka, S. Haj Ibrahim, T. Wejrzanowski, *Materials* 12 (2019), 2017.
- [36] N. Xu, X. Hu, W. Xu, X. Li, L. Zhou, S. Zhu, J. Zhu, *Adv. Mater.* 29 (2017) 1606762.
- [37] W. Xu, X. Hu, S. Zhuang, Y. Wang, X. Li, L. Zhou, S. Zhu, J. Zhu, *Adv. Energy Mater.* 8 (2018), 1702884.
- [38] M. Ye, J. Jia, Z. Wu, C. Qian, R. Chen, P.G. O'Brien, W. Sun, Y. Dong, G.A. Ozin, *Adv. Energy Mater.* 7 (2017), 1601811.
- [39] R. Li, L. Zhang, L. Shi, P. Wang, *ACS Nano* 11 (2017) 3752–3759.
- [40] J. Wang, Y. Li, L. Deng, N. Wei, Y. Weng, S. Dong, D. Qi, J. Qiu, X. Chen, T. Wu, *Adv. Mater.* 29 (2017), 1603730.
- [41] J. Yang, Y. Pang, W. Huang, S.K. Shaw, J. Schiffbauer, M.A. Pillers, X. Mu, S. Luo, T. Zhang, Y. Huang, G. Li, S. Ptasinska, M. Lieberman, T. Luo, *ACS Nano* 11 (2017) 5510–5518.
- [42] G. Wang, Y. Fu, X. Ma, W. Pi, D. Liu, X. Wang, *Carbon* 114 (2017) 117–124.
- [43] X. Hu, W. Xu, L. Zhou, Y. Tan, Y. Wang, S. Zhu, J. Zhu, *Adv. Mater.* 29 (2017) 1604031.
- [44] P. Mu, Z. Zhang, W. Bai, J. He, H. Sun, Z. Zhu, W. Liang, A. Li, *Adv. Energy Mater.* 9 (2019), 1802158.
- [45] Y. Zhang, S.K. Ravi, L. Yang, J.V. Vaghasiya, L. Suresh, I. Tan, S.C. Tan, *ACS Appl. Mater. Interfaces* 11 (2019) 38674–38682.